

LM-CartSeg: Automated Segmentation of Lateral and Medial Cartilage and Subchondral Bone for Radiomics Analysis

Tongxu Zhang^a

^a*Department of Rehabilitation Sciences, The Hong Kong Polytechnic University, Kowloon, Hong Kong, China*

Abstract

Background and Objective: Radiomics of knee MRI requires robust, anatomically meaningful regions of interest (ROIs) that jointly capture cartilage and subchondral bone. Most existing work relies on manual ROIs and rarely reports quality control (QC). We present LM-CartSeg, a fully automatic pipeline for cartilage/bone segmentation, geometric lateral/medial (L/M) compartmentalization and radiomics analysis.

Methods: Two 3D nnU-Net models were trained on SKM-TEA (138 knees) and OAIZIB-CM (404 knees). At test time, zero-shot predictions were fused and refined by simple geometric rules: connected-component cleaning, construction of 10 mm subchondral bone bands in physical space, and a data-driven tibial L/M split based on PCA and k -means. Segmentation was evaluated on an OAIZIB-CM test set (103 knees) and on SKI-10 (100 knees). QC used volume and thickness signatures. From 10 ROIs we extracted 4 650 non-shape radiomic features to study inter-compartment similarity, dependence on ROI size, and OA vs. non-OA classification on

Results: Post-processing improved macro ASSD on OAIZIB-CM from 2.63 to 0.36 mm and HD95 from 25.2 to 3.35 mm, with DSC ≈ 0.91 ; zero-shot DSC on SKI-10 was ≈ 0.80 . The geometric L/M rule produced stable compartments across datasets, whereas a direct L/M nnU-Net showed domain-dependent side swaps. Only 6–12% of features per ROI were strongly correlated with volume or thickness. Radiomics-based models restricted to size-linked features.

Conclusions: LM-CartSeg yields automatic, QC'd ROIs and radiomic features that carry discriminative information beyond simple morphometry, providing a practical foundation for multi-centre knee OA radiomics studies.

Keywords: Knee MRI, Cartilage segmentation, Subchondral bone, Knee osteoarthritis, Radiomics, nnU-Net

1. Introduction

Knee osteoarthritis (KOA) is one of the most prevalent musculoskeletal disorders worldwide and a leading cause of pain, disability, and loss of quality of life in older adults. Recent Global Burden of Disease analyses estimate that osteoarthritis affected roughly 595 million people in 2020, corresponding to about 7.6% of the global population, with knee involvement accounting for a large and rapidly growing share of cases [1, 2]. The incidence and prevalence of KOA continue to rise in parallel with population ageing and obesity, posing substantial socioeconomic and healthcare challenges.

Magnetic resonance imaging (MRI) provides a three-dimensional, multi-tissue view of the knee joint, enabling direct assessment of articular cartilage, menisci, and subchondral bone [3, 4]. Quantitative sequences such as T_2 and $T_{1\rho}$ mapping can detect biochemical alterations in cartilage before radiographic damage appears, and have been associated with subsequent development or progression of KOA [5, 6].

Radiomics, the high-throughput extraction of large numbers of quantitative features from medical images—has been proposed as a bridge between medical imaging and precision medicine [7, 8]. By systematically quantifying intensity, texture, and shape patterns, radiomic features can capture subtle tissue alterations that are invisible to the naked eye and may carry prognostic or predictive information. In KOA, MRI-based radiomics frameworks have been developed to identify OA using features from cartilage, subchondral bone, and other joint tissues,[9, 10, 11, 12, 13, 14] to predict structural or symptomatic progression, and to construct multi-tissue signatures that integrate cartilage and subchon-

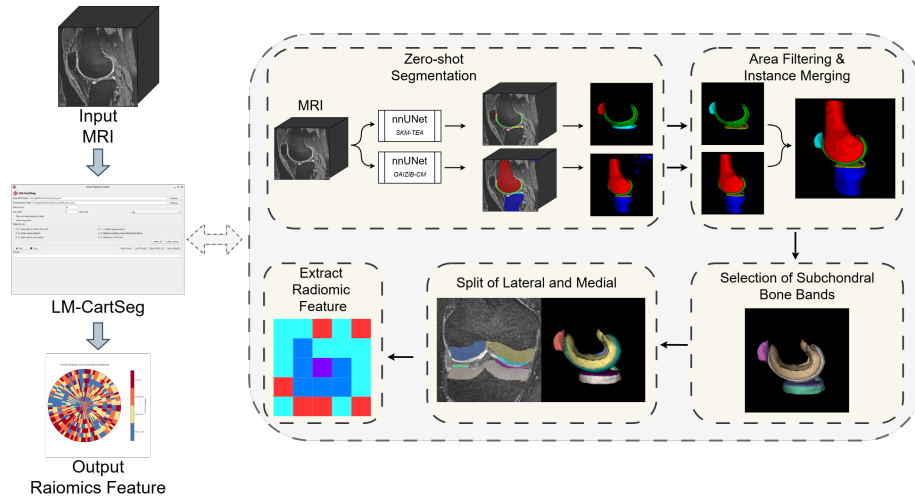


Figure 1: Overview of the proposed pipeline: LM-CartSeg. A 3D knee MR volume is processed by two pretrained nnU-Net models (SKM-TEA and OAI/ZIB-CM) for zero-shot segmentation, followed by area filtering and instance merging to obtain clean cartilage and bone labels. Femoral and tibial cartilage are then split into lateral and medial compartments, subchondral bone bands are generated, and radiomic features are extracted for downstream analysis.

dral bone information. These studies demonstrate the potential of radiomics for early KOA assessment but also highlight important methodological challenges.

Their main focus is on the cartilage [11, 15], subchondral bone [9, 16] or both of them [17, 10]. However, most of these tasks require the involvement of doctors or radiologists in manual ROI segmentation. Therefore, it is necessary to propose an automatic segmentation of cartilage and subchondral bone to reduce human consumption. And this method can be used for lateral and medial cartilage, and the thickness of subchondral bone should be set according to specific requirements.

Recent advances in deep learning have enabled robust automatic segmentation in medical imaging [18, 19, 20, 21, 22], including applications to knee bones and cartilage on MRI. Ambellan et al. [23] introduced a framework that combines 3D statistical shape models with 2D/3D convolutional neural networks to segment femur, tibia, and cartilage compartments in Osteoarthritis Initiative (OAI) data, forming the basis of the OAIZIB-CM dataset. Subsequent work

has extended these ideas to fully automatic cartilage subregional assessment and to heterogeneous clinical MRI protocols [24]. However, most existing KOA radiomics studies [25, 26, 27] still analyze either cartilage or subchondral bone in isolation, often in a limited number of compartments, and rarely exploit fully automatic, anatomically detailed regions-of-interest (ROIs) that jointly cover lateral/medial (L/M) cartilage and the corresponding subchondral bone bands.

In this work, we build on automatic segmentation to construct an end-to-end, fully automated pipeline for knee radiomics analysis (Fig. 1). Starting from routine 3D knee MRI, we:

- automatically segment femoral, tibial, and patellar cartilage in 3D;
- derive *subchondral bone bands* of fixed physical thickness inside the femur and tibia, measured inward from the cartilage–bone interface;
- partition femoral/tibial cartilage and their subchondral bands into lateral (L) and medial (M) compartments using a purely geometric rule that generalizes across cohorts;
- extract standardized radiomics features from all cartilage and subchondral ROIs.

We systematically evaluate segmentation accuracy and the robustness of the L/M partition across three cohorts, and use simple morphometric quantities (volume, mean thickness, and compartmental ratios) as sanity checks and quality-control indicators. Within each cohort, we further compare OA classification performance between size-linked descriptors (volume/thickness) and texture radiomics to quantify the incremental value of texture under a realistic, fully automatic pipeline, rather than to build a cross-center deployable classifier.

2. Methods

2.1. Network training and inference by nnU-Net

We adopt the 3D full-resolution nnU-Net framework the state-of-the-art segmentation model in medical imaging[18, 21] to segment femoral, tibial and patel-

lar cartilage and the corresponding bones. Two models are trained independently on the public SKM-TEA [28] and OAIZIB-CM [23, 24] datasets, respectively, using the provided manual labels as ground truth. The label sets differ slightly: SKM-TEA provides femoral and patellar cartilage, bilateral menisci and bilateral tibial cartilage, whereas OAIZIB-CM provides femur, femoral cartilage, tibia and bilateral tibial cartilage.

For each dataset, nnU-Net uses its default preprocessing, resampling to a dataset-specific target spacing and z -score intensity normalization [29, 30, 31]. Also default data augmentations, like random flips, rotations, scalings and intensity transforms. And the standard combined Dice and cross-entropy loss. Among them, the hyperparameters for training, except for the epoch multiple set to 250 rounds, are automatically optimized by nnU-Net. Training and validation splits are defined at the subject level to avoid information leakage.

At test time, we run both trained models with the default nnU-Net inference settings, such as sliding-window prediction with test-time mirroring, and obtain one softmax probability map per model. These probability maps are fused in probability space (voxelwise averaging), and the final hard labels are obtained by voxelwise argmax followed by connected-component filtering and anatomical instance merging.

2.2. Geometric post-processing and explainable rules

Starting from the voxelwise nnU-Net predictions, we apply a sequence of fully rule-based geometric post-processing steps to obtain anatomically plausible, analysis-ready masks. This includes connected-component cleaning to remove obvious segmentation errors, construction of fixed-thickness subchondral bone bands, and a data-driven yet anatomically interpretable partition of lateral (L) and medial (M) compartments, as shown in Fig. 2.

Connected-component cleaning. For each anatomical label, we compute 3D connected components (6-connectivity). We apply label-specific, interpretable rules:

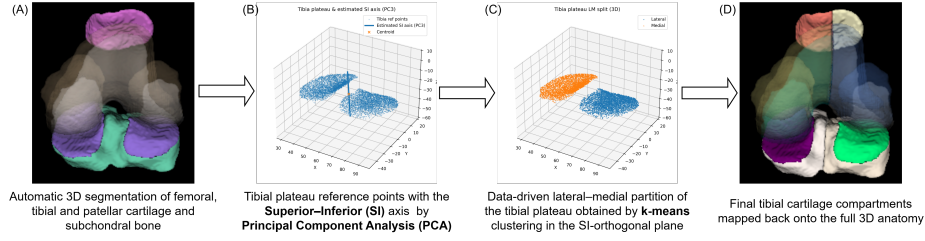


Figure 2: Data-driven tibial compartment definition: (A) Segmented cartilage and subchondral bone, (B) PCA [32] derived superior–inferior axis, (C) k-means [33] lateral–medial partition in the SI-orthogonal plane, (D) Resulting tibial compartments on the 3D anatomy.

- **Bones:** keep the largest component near the volume center; optionally discard components touching the acquisition borders.
- **Cartilage:** keep all components with size \geq a minimum threshold. Thresholds are specified in physical volume (mm^3) and converted to voxels via $n_{\min} = \lfloor V_{\min}/(s_x s_y s_z) \rfloor$, where (s_x, s_y, s_z) are voxel sizes in mm.

Subchondral bone bands. Let $B(x) \in \{0, 1\}$ denote the bone mask (femur or tibia), $C(x) \in \{0, 1\}$ the corresponding cartilage mask, and $\mathbf{s} = (s_x, s_y, s_z)$ the voxel spacing in mm. We compute the Euclidean distance transform (EDT) on the complement of cartilage with physical sampling:

$$D(x) = \min_{y: C(y)=1} \|(x - y) \odot \mathbf{s}\|_2. \quad (1)$$

For a target band thickness $t \in \{5, 10\}$ mm, which could be set in the UI to choose others thickness, the subchondral band is defined as

$$\Omega_{\text{sub}} = \{x \mid B(x) = 1 \wedge D(x) \leq t\}. \quad (2)$$

This yields a geometrically meaningful layer restricted to bone and equidistant (in mm) from the cartilage interface.

Lateral/Medial (L/M) compartment partition. For each knee we derive a case-specific L/M boundary directly from the tibial plateau geometry. Let $\Omega_{\text{ref}} \subset \mathbb{Z}^3$ denote a tibial reference mask and $\{x_i\}_{i=1}^N \subset \mathbb{R}^3$ the corresponding world-coordinate points obtained from the image affine.

1. **Reference region.** We preferentially take Ω_{ref} as the tibial cartilage mask; if it contains fewer than 200 voxels ($N < 200$), we fall back to the tibial subchondral band. This yields a point cloud $X = \{x_i\}_{i=1}^N$ sampling the tibial plateau.
2. **Local plane via PCA.** We compute the centroid $c = \frac{1}{N} \sum_{i=1}^N x_i$ and fit a 3D PCA to X . Let (e_1, e_2, e_3) be the eigenvectors of the sample covariance matrix $\Sigma = \frac{1}{N} \sum_{i=1}^N (x_i - c)(x_i - c)^\top$, ordered by decreasing eigenvalue. The third principal axis $s = e_3/\|e_3\|$ is used as an approximation of the superior–inferior (SI) direction. We remove the SI component,

$$x_i^\perp = (x_i - c) - ((x_i - c)^\top s)s,$$

and perform a second PCA on $\{x_i^\perp\}$ to obtain two orthonormal in-plane axes $u, v \in \mathbb{R}^3$. Each point is then represented in local planar coordinates

$$(u_i, v_i) = (u^\top (x_i - c), v^\top (x_i - c)) \in \mathbb{R}^2.$$

3. **Planar clustering.** On the 2D coordinates $z_i = (u_i, v_i)$ we run k -means with $k = 2$, obtaining a partition $\{1, 2\}$ that minimizes within-cluster variance and cluster centroids $\mu_1, \mu_2 \in \mathbb{R}^2$. These centroids are mapped back to world coordinates as

$$\tilde{x}_j = c + \mu_{j,1}u + \mu_{j,2}v, \quad j \in \{1, 2\},$$

and assigned to lateral vs. medial using the scanner left–right axis and the known laterality (L/R) of the knee: for a left knee the cluster with larger x -coordinate is labelled lateral, whereas for a right knee it is the opposite.

4. **Consistent partitioning of all masks.** The fitted k -means model in (u, v) -space is then reused for all relevant masks (femoral/tibial cartilage and their subchondral bands). For any voxel y in these masks we compute its planar coordinates (u_y, v_y) as above, predict its cluster label with the same k -means model, and map it to the corresponding L/M compartment. This yields a single, case-specific L/M boundary that is applied consistently across all structures.

This constitutes a *rules + unsupervised* scheme: PCA and k -means adapt to the individual tibial geometry, while simple laterality rules provide anatomical semantics (lateral vs. medial). Unlike template- or atlas-based cartilage partitioning methods that rely on predefined radial transformations and elastic registration [34, 27], our L/M boundary is obtained directly from the patient’s tibial shape without any template.

2.3. Regions of interest (ROIs)

All radiomics analyses are based on the final, post-processed 3D masks obtained in Sections 2.1–2.2. From the femoral and tibial bone masks and their corresponding cartilage masks, we derive fixed-thickness subchondral bone bands using the Euclidean distance transform in millimetres. For radiomics, we focus on $t = 10$ mm bands to align with prior work on subchondral bone radiomics in knee OA [12, 10]. All cartilage and subchondral structures are further split into lateral (L) and medial (M) compartments using the case-specific geometric L/M boundary.

Because the SKM-TEA and OAIZIB-CM models have slightly different label sets, we map their outputs to a common set of radiomics ROIs and do not use the meniscal labels from SKM-TEA in the present analysis. This yields, for each knee, the following primary ROIs:

- Femoral cartilage (FC), split into LF and MF.
- Tibial cartilage (TC), split into LT and MT.
- Patellar cartilage (PC), split into LP and MP.
- Femoral subchondral bone band, split into LF_SUB and MF_SUB.
- Tibial subchondral bone band, split into LT_SUB and MT_SUB.

These ROIs provide anatomically interpretable subregions covering both articular cartilage and the immediately underlying subchondral bone, which are expected to jointly capture OA-related morphological and textural changes.

3. Segmentation Experiments

3.1. Environment Settings

All the code runs within the Ubuntu 22.04.3 LTS on Windows 10 x86_64 operating system, with an NVIDIA GeForce RTX 4060 Ti GPU, and utilizes the PyTorch framework. The code for LM-CartSeg can be accessed at <https://github.com/jukieCheung/LM-CartSeg>. The code for nnU-Net can be accessed at <https://github.com/MIC-DKFZ/nnU-Net>.

3.2. Datasets and splits

We train two separate 3D nnU-Net models [18, 21] on the training portions of SKM-TEA [28] and OAIZIB-CM [23, 24], respectively. The SKM-TEA training split contains 138 knee MR volumes, while the OAIZIB-CM training split contains 404 volumes. All splits are defined case-wise to ensure that no subject contributes scans to both training and evaluation.

To assess *cross-domain* and *zero-shot* generalisation, we apply the trained models without any fine-tuning to three additional cohorts: the SKI-10 challenge dataset [35] that includes 100 knees with expert ground truth, an official test set of OAIZIB-CM cohort knee MR scans. SKI-10 and the held-out OAIZIB-CM cohort are used to evaluate segmentation performance in genuinely out-of-distribution primarily used to study the clinical translation of downstream volume and radiomics analyses under zero-shot segmentation.

3.3. Preprocessing

In geometry, we resample all images to a common voxel spacing is applied to (256, 256, 160), where x=coronal, y=axial, z=sagittal, only when needed; all geometric operations (distance thresholds and band thickness) are defined in *millimeters* to decouple them from resampling.

3.4. Evaluation protocol

Segmentation accuracy. On OAI-ZIB-CM and SKI-10 we evaluate the automatic segmentations using standard overlap and surface metrics: Dice similarity coefficient (DSC), 95th-percentile Hausdorff distance (HD95), and average symmetric surface distance (ASSD). [36, 37] For a given structure with ground-truth label set G and predicted label set P , the DSC is

$$\text{DSC}(G, P) = \frac{2|G \cap P|}{|G| + |P|}. \quad (3)$$

Surface-based distances are computed on the corresponding object surfaces ∂G and ∂P . Let $d(x, \partial P)$ denote the minimal Euclidean distance from a point x on ∂G to ∂P (and analogously $d(y, \partial G)$ for $y \in \partial P$). The *directed* surface distance distributions are

$$D_{G \rightarrow P} = \{d(x, \partial P) : x \in \partial G\}, \quad D_{P \rightarrow G} = \{d(y, \partial G) : y \in \partial P\}. \quad (4)$$

We then define

$$\text{HD95}(G, P) = \max\{\text{percentile}_{95}(D_{G \rightarrow P}), \text{percentile}_{95}(D_{P \rightarrow G})\}, \quad (5)$$

$$\text{ASSD}(G, P) = \frac{1}{|\partial G| + |\partial P|} \left(\sum_{x \in \partial G} d(x, \partial P) + \sum_{y \in \partial P} d(y, \partial G) \right). \quad (6)$$

These metrics are computed per structure (femur, tibia, patella, femoral cartilage, tibial cartilage, patellar cartilage, and 10 mm subchondral bands) using a common evaluation script based on surface-distance calculations, and summarised as case-wise macro averages over labels:

$$\overline{\text{DSC}}^{(i)} = \frac{1}{L} \sum_{\ell=1}^L \text{DSC}(G_{\ell}^{(i)}, P_{\ell}^{(i)}), \quad (7)$$

for case i and L evaluated labels.

L/M partition accuracy. To assess the quality of the lateral/medial (L/M) split of femoral and tibial cartilage, we compare two strategies under identical ground truth: (A) a direct nnU-Net trained to predict L/M compartments as the *pred*, and (B) our two-stage approach that first segments whole cartilage and then

applies a geometric L/M partition as the *GT*. Let Ω denote the set of voxels in the tibial cartilage region of interest, and let $y^{\text{GT}}(v) \in \{\text{LT}, \text{MT}\}$ and $y^{\text{pred}}(v) \in \{\text{LT}, \text{MT}\}$ denote the ground-truth and predicted L/M labels for voxel $v \in \Omega$. The overall L/M accuracy is

$$\text{ACC}_{\text{LM}} = \frac{1}{|\Omega|} \sum_{v \in \Omega} \mathbb{I}(y^{\text{GT}}(v) = y^{\text{pred}}(v)), \quad (8)$$

and class-wise precision/recall are derived from the usual confusion counts for LT and MT.

To quantify mixing along the inter-compartment boundary, we define a *boundary confusion* rate. Let Γ be a one-voxel-wide band around the LT/MT interface (e.g. the union of dilated LT and MT surfaces). The symmetric boundary confusion is

$$\text{BC} = \frac{1}{|\Gamma|} \sum_{v \in \Gamma} \mathbb{I}(y^{\text{GT}}(v) \neq y^{\text{pred}}(v)), \quad (9)$$

and directional confusion (LT \rightarrow MT, MT \rightarrow LT) is obtained by restricting the sum to voxels with $y^{\text{GT}}(v) = \text{LT}$ or $= \text{MT}$, respectively. Alongside per-compartment DSC and HD95 for LF/MF and LT/MT, these measures quantify how much the predicted L/M labels “leak” across the anatomical boundary when comparing direct L/M prediction to our geometric partition.

Anatomical quality control (QC). Beyond voxelwise overlap, we perform automatic anatomical QC on all predicted 10 mm cartilage and subchondral bone bands, inspired by prior work on segmentation quality control [37, 38, 39, 40]. For a region of interest R with voxel set \mathcal{V}_R and voxel volume Δv , the anatomical volume is

$$V_R = |\mathcal{V}_R| \Delta v. \quad (10)$$

Let A_R denote the surface area of R obtained from a triangulated surface mesh (e.g. marching cubes). A simple global thickness estimate is then

$$\bar{T}_R = \frac{2V_R}{A_R}, \quad (11)$$

and, when needed, local thickness distributions are summarised using percentiles of a 3D Euclidean distance transform inside R (e.g. T_{10} , T_{50} , T_{90}).

For lateral–medial comparisons, we compute thickness ratios and differences, for example for tibial cartilage

$$r_{\text{TIB}} = \frac{\bar{T}_{\text{MT}}}{\bar{T}_{\text{LT}}}, \quad \Delta_{\text{TIB}} = \bar{T}_{\text{MT}} - \bar{T}_{\text{LT}}, \quad (12)$$

and analogously for femoral cartilage. At the cohort level, we inspect the distributions of V_R , \bar{T}_R , r_{TIB} and r_{FEM} (means, standard deviations and coefficients of variation) and perform paired Wilcoxon tests for LT–MT and LF–MF comparisons. Cases with implausible morphometry (e.g. extremely small V_R , extreme \bar{T}_R or thickness ratios far from 1) are flagged as outliers for visual review. These QC checks ensure that the automatically generated ROIs are not only accurate with respect to the reference segmentations, but also anatomically plausible across datasets.

4. Radiomics Experiments

4.1. Datasets and labels

Radiomic analysis was performed on the held-out official test set of the OAIZIB-CM with 103 knees [23, 24]. For OAIZIB-CM, Kellgren–Lawrence (KL) grades are provided as part of the metadata, enabling supervised learning with osteoarthritis (OA) labels. Following common practice, we defined a binary outcome *radiographic OA* as

$$\text{OA} = \begin{cases} 1, & \text{if } \text{KL} \geq 2, \\ 0, & \text{if } \text{KL} \leq 1. \end{cases}$$

reviewed the radiology reports and used the presence of phrases such as “*osteoarthritic changes*”, “*degenerative changes*”, “*marginal osteophytes*”, or “*patellofemoral osteoarthritic changes*” as an imaging-report–defined OA indicator. Subjects whose reports contained at least one of these phrases were labelled as OA; all others were labelled as non-OA. This definition is not a gold standard, but is used as a pragmatic, imaging-derived phenotype for exploratory analysis and for assessing the behaviour of our automated pipeline on non-OAI data.

Unless otherwise stated, quantitative classification experiments and dataset was used to qualitatively assess the external behaviour of selected signatures and their feature distributions.

4.2. Feature extraction

All radiomic features are computed on the original MR images used in the segmentation pipeline, including 3D DESS-like [23, 24, 35], T₂-weighted, fat-suppressed sequences), rather than on quantitative T₂ maps. This differs from some prior knee OA radiomics work based on T₂ mapping [41, 42], and may partly explain differences in absolute feature values and discriminative performance.

Within each ROI, we extract a standard panel of IBSI-compliant handcrafted radiomic features using an open-source library: PyRadiomics [43], to:

- **Gray-level discretisation:** intensities are discretised using a fixed bin width: 5 gray levels, harmonised to the dynamic range of the sequence [44].
- **First-order statistics:** histograms and intensity summary measures (mean, median, percentiles, skewness, kurtosis, energy, etc.).
- **Texture features:** gray-level co-occurrence matrix (GLCM), run-length matrix (GLRLM), size-zone matrix (GLSZM), neighbourhood gray-tone difference matrix (NGTDM), and gray-level dependence matrix (GLDM) features, computed on the discretised images.
- **Filtered features:** the above first-order and texture features are also computed on filtered versions of the images, including logarithmic (LoG) filters and multi-scale wavelet decompositions, thereby capturing multi-scale texture patterns.

Shape features are extracted for completeness but, as discussed below, they are excluded from the primary radiomics signatures due to their low robustness under segmentation perturbations and redundancy with simpler morphological

measures (e.g. volume). Unless otherwise noted, all classification models in Section 4.3 are built on non-shape radiomic features.

4.3. Feature selection and classification

To distinguish OA ($KL \geq 2$) from non-OA knees in the OAI-ZIB-CM test set, we explore several supervised classification pipelines that combine feature selection with regularised classifiers. All models are evaluated using stratified k -fold cross-validation (typically $k = 5$), and performance is reported as the mean area under the ROC curve (AUC) and accuracy across folds.

Statistical feature selection pipelines. We consider a statistical feature selection schemes motivated by existing radiomics studies:

- **Xue-style pipeline.** [10] As an alternative, we first apply LASSO logistic regression [45] to the full non-shape feature set to obtain a preliminary sparse subset. For these selected features, we then perform Mann-Whitney U tests to retain only those with significant group differences and optionally remove highly collinear features using a correlation threshold (e.g. Pearson $|r| > 0.9$).

These baselines reflect conventional radiomics practice where feature selection is driven purely by predictive performance and statistical significance, without explicit robustness considerations.

Classifiers and evaluation. For each selected feature set, we train the L1-regularised logistic regression (LASSO), which simultaneously performs feature selection.

Hyperparameters are set as default. For each model and feature set, we record 5 folds cross-validated AUC and accuracy.

Together, these experiments position our work within the broader radiomics framework: starting from fully automatic, anatomically guided ROIs, we systematically examine the interplay between segmentation robustness, feature selection strategy, and downstream classification performance for MRI-based knee OA assessment.

Table 1: Macro-averaged segmentation metrics on the OAIZIB-CM test set (103 knees) before and after geometric post-processing. Δ denotes $\text{clear_seg} - \text{seg}$.

Metric	seg	clear_seg	Δ	Wilcoxon p
DSC \uparrow	0.892	0.907	+0.015	4.5×10^{-10}
ASSD [mm] \downarrow	2.63	0.36	-2.26	1.3×10^{-18}
HD95 [mm] \downarrow	25.16	3.35	-21.81	2.4×10^{-18}

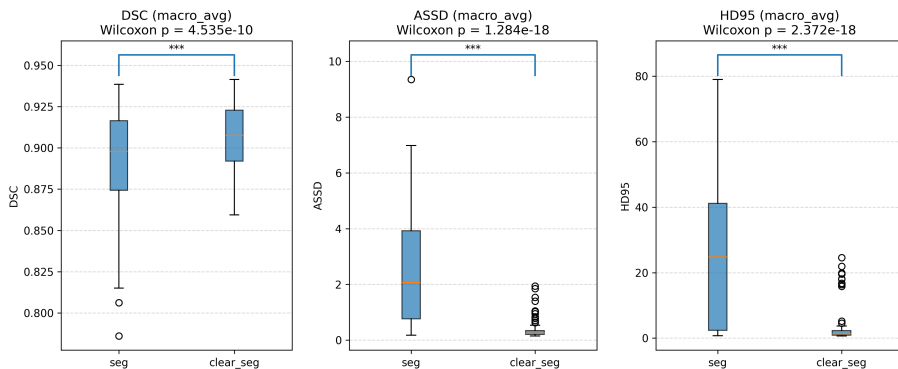


Figure 3: Macro-averaged DSC, ASSD and HD95 on the OAIZIB-CM test set, comparing raw nnU-Net segmentations (seg) with post-processed masks (clear_seg). Brackets indicate paired Wilcoxon p -values.

5. Segmentation Results

5.1. Training and in-domain validation

The two 3D nnU-Net models converged stably on their respective training cohorts. On SKM-TEA, the mean validation Dice similarity coefficient (DSC) across all labels was 0.867, while on OAIZIB-CM it reached 0.916, indicating accurate multi-structure segmentation on both datasets.

5.2. Segmentation accuracy on the OAIZIB-CM test set

On the official OAIZIB-CM test cohort (103 knees), we compared the raw nnU-Net predictions with the geometrically cleaned LM-CartSeg outputs, using case-wise macro-averaged DSC, average symmetric surface distance (ASSD)

Table 2: Macro-averaged zero-shot segmentation performance on the SKI-10 dataset (100 knees). Values are means across cases; Δ denotes `clear_seg - seg`.

Metric	seg	clear_seg	Δ	Wilcoxon p
DSC \uparrow	0.796	0.797	+0.001	3.3×10^{-5}
ASSD [mm] \downarrow	1.07	0.94	-0.13	1.3×10^{-5}
HD95 [mm] \downarrow	7.59	6.13	-1.46	1.8×10^{-1}

and 95th-percentile Hausdorff distance (HD95) over the four evaluated structures. As summarised in Table 1 and Figure 3, the post-processing step substantially improved surface agreement: mean ASSD decreased from 2.63 mm to 0.36 mm and mean HD95 from 25.2 mm to 3.35 mm, while the mean DSC increased from 0.892 to 0.907. Paired Wilcoxon signed-rank tests on the macro-averaged metrics confirmed that these improvements were highly significant (DSC $p = 4.5 \times 10^{-10}$, HD95 $p = 2.4 \times 10^{-18}$, ASSD $p = 1.3 \times 10^{-18}$).

Label-wise analyses showed the same pattern for three out of four structures, with consistent and significant gains in all metrics; for the remaining structure, DSC was statistically unchanged (Wilcoxon $p = 0.12$) but HD95 and ASSD still improved markedly after post-processing. Overall, these results demonstrate that the geometric cleaning and instance-merging rules lead to systematically smoother and more anatomically plausible segmentations without sacrificing overlap accuracy.

5.3. Zero-shot performance on SKI-10

We further evaluated cross-domain generalisation on the SKI-10 challenge cohort (100 knees), where neither images nor labels were seen during training. In this strictly zero-shot setting, the raw nnU-Net predictions already achieved a macro-averaged DSC of 0.796, ASSD of 1.07 mm and HD95 of 7.59 mm across the four evaluated structures.

After applying the proposed geometric cleaning and instance-merging rules, macro-averaged ASSD improved from 1.07 mm to 0.94 mm and HD95 from 7.59 mm to 6.13 mm, while DSC increased slightly from 0.796 to 0.797. Nu-

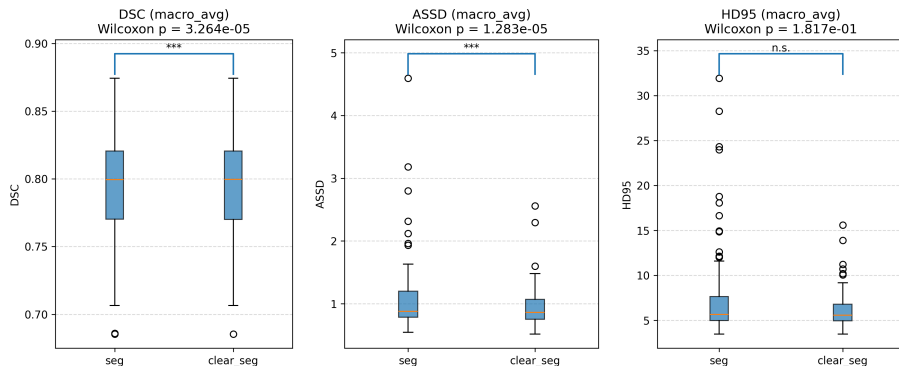


Figure 4: Zero-shot macro-averaged DSC, ASSD and HD95 on the SKI-10 dataset, comparing seg vs. clear_seg. Brackets show paired Wilcoxon p -values; HD95 differences are not significant.

merical results are summarised in Table 2, with the corresponding distributions shown in Figure 4. Paired Wilcoxon tests on the macro-averaged metrics showed significant gains in DSC ($p = 3.3 \times 10^{-5}$) and ASSD ($p = 1.3 \times 10^{-5}$), whereas the HD95 reduction did not reach statistical significance ($p = 0.18$).

Label-wise analysis revealed that two large structures reached DSC values above 0.96 in the zero-shot setting, while the two smaller structures remained more challenging (DSC \approx 0.56–0.68). For three of the four labels, post-processing significantly improved at least one of DSC, ASSD or HD95, and for the remaining label the overlap was preserved while surface distances still decreased.

Overall, these results indicate that the proposed geometric rules consistently enhance surface accuracy without degrading overlap, even on a dataset that is markedly different from the training domain.

5.4. Accuracy of the learned L/M tibial partition

We compared our rule-based two-stage L/M partition against a direct nnU-Net trained to predict lateral tibial (LT) and medial tibial (MT) cartilage as separate labels. In the two-stage scheme, nnU-Net segments the whole tibial cartilage and the L/M split is imposed afterwards by the geometric rule from

Table 3: Voxel-wise LT/MT classification performance of the direct L/M nnU-Net relative to the geometric L/M partition on the tibial plateau. Values are mean \pm SD across knees, reported as percentages.

Accuracy (ACC)	99.9 \pm 0.4	92.1 \pm 15.2	93.6 \pm 21.9
Balanced accuracy	100.0 \pm 0.4	92.0 \pm 14.6	93.6 \pm 21.8
LT \rightarrow MT confusion	0.0 \pm 0.2	9.5 \pm 22.1	0.3 \pm 2.0
MT \rightarrow LT confusion	0.1 \pm 0.6	4.8 \pm 14.3	1.5 \pm 5.4
Symmetric confusion (CONF_sym)	0.0 \pm 0.4	7.2 \pm 13.8	0.9 \pm 2.8

Section 2.2; by construction, this partition cannot swap sides and serves as a deterministic reference as the *GT*). The direct L/M nnU-Net as the *pred* is always evaluated against this GT.

On the in-domain OAIZIB-CM test set, the direct L/M network closely reproduces the geometric partition, as shown in Figure 5. DSC, ASSD and HD95 are high and tightly distributed for both LT and MT, with LT being slightly easier (all Wilcoxon $p < 10^{-2}$). Voxel-wise L/M classification on the tibial plateau confirms this: the mean accuracy is 99.95% \pm 0.42% and the balanced accuracy 99.95% \pm 0.39%, with per-side precision/recall all above 99.9%. The mean symmetric boundary confusion rate is only 0.05% \pm 0.38%, and there is no significant asymmetry between LT \rightarrow MT and MT \rightarrow LT errors, as shown in Table 3. Thus, within the training domain, a network can effectively learn the same L/M split as the geometric rule.

learned L/M labels are much less robust under domain shift. On SKI-10, many knees still achieve high DSC with respect to the geometric GT, but there are several clear outliers with DSC near zero for one compartment, indicating almost complete side swaps. The corresponding boundary confusion distributions are heavy-tailed, with some cases exhibiting substantial fractions of tibial-plateau voxels assigned to the wrong per-side DSC distributions are broad with many low values, ASSD and HD95 are highly variable, and the symmetric confusion rate can reach > 0.3 in difficult scans. Moreover, LT \rightarrow MT errors are consistently larger than MT \rightarrow LT, revealing a systematic directional bias.

Overall, these results suggest that while a direct L/M nnU-Net can mimic the

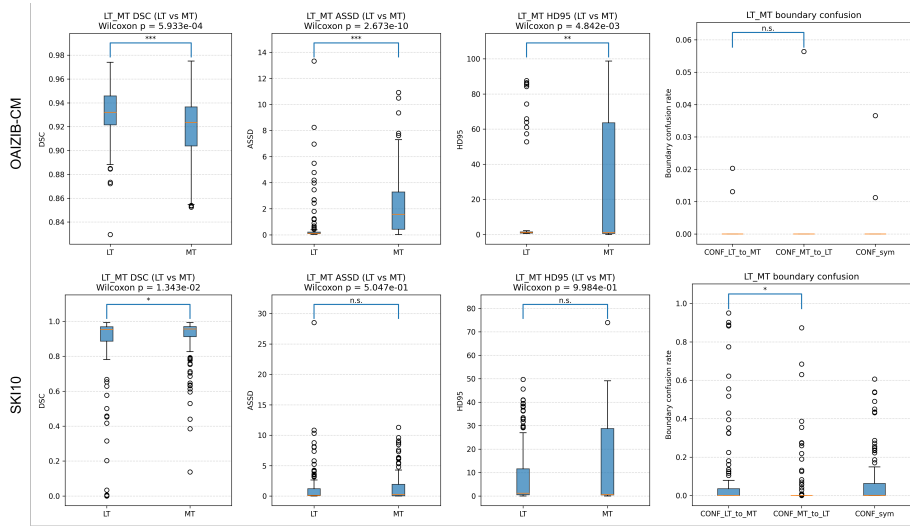


Figure 5: Accuracy of the learned tibial L/M partition across datasets. Rows (top to bottom) show OAI3B-CM (in-domain), SKI-10 (zero-shot) and geometric L/M partition. Columns (left to right) display per-side DSC, ASSD and HD95 for LT vs. MT, and voxel-wise L/M boundary confusion (CONF_LT_to_MT, CONF_MT_to_LT, CONF_sym). Brackets indicate paired Wilcoxon p -values. The learned L/M labels closely match the geometric partition in-domain, but become unstable and asymmetric under domain

Table 4: Anatomical QC: lateral/medial tibial and femoral cartilage thickness asymmetry across datasets. Values are mean \pm SD across knees; ratios are medial/lateral, and Δt is medial minus lateral thickness in mm (negative values indicate thinner medial cartilage).

Dataset	Tibia ratio	Tibia Δt (mm)	Femur ratio	Femur Δt (mm)
OAI-ZIB-CM (n=103)	0.88 \pm 0.14	-0.24 \pm 0.25	0.96 \pm 0.07	-0.08 \pm 0.15
SKI-10 (n=100)	0.86 \pm 0.21	-0.30 \pm 0.36	0.99 \pm 0.09	-0.04 \pm 0.20

geometric partition when train and test domains match, its L/M labels become unreliable and biased on out-of-distribution data. In contrast, the proposed geometric L/M rule is deterministic, annotation-free and domain-agnostic, and is therefore adopted as the default partition strategy in our downstream radiomics pipeline.

5.5. Anatomical quality control (QC)

To verify that the automatically derived ROIs preserve plausible knee anatomy, we performed simple QC analyses on the 10 mm tibial and femoral cartilage bands across all three cohorts. For each knee we computed the volume and mean thickness of the lateral and medial tibial cartilage (LT, MT) and femoral cartilage (LF, MF), as well as the medial-to-lateral thickness ratios (TIB_ratio, FEM_ratio). LT–MT and LF–MF pairs were compared with paired Wilcoxon tests as shown in Figure 6, and summary statistics are reported in Table 4.

the expected asymmetry: medial tibial cartilage was smaller and thinner than lateral cartilage. Mean LT volumes exceeded MT volumes in every dataset, such as 2379 vs. 2133 mm³ in OAI; 2288 vs. medial–lateral thickness differences were around -0.25 to -0.30 mm, TIB_ratio \approx 0.86–0.88 in all three cohorts, all $p \ll 0.001$. These consistent patterns across domains argue against systematic L/M swapping or gross geometric artefacts in the tibial compartments.

Femoral cartilage displayed a more balanced L/M morphology, again in line with prior anatomical observations. Medial and lateral femoral volumes were similar that LF and MF within $\sim 10\%$ in all cohorts, and mean thicknesses differed only slightly, with FEM_ratio close to 1. The LF–MF thickness difference was significant only in OAI, and non-significant in SKI-10 and bias on

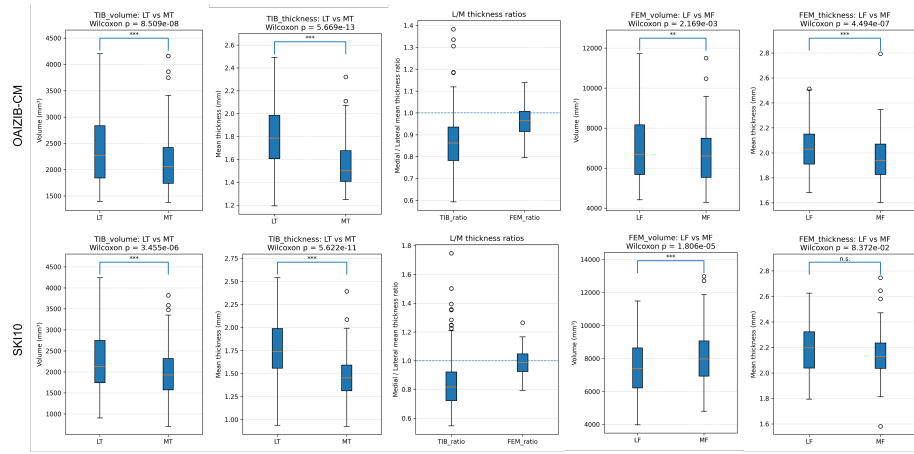


Figure 6: Anatomical QC of 10 mm cartilage bands across datasets. right) show tibial cartilage volume (LT vs. MT), tibial mean thickness, medial/lateral tibial and femoral thickness ratios, femoral cartilage volume (LF vs. MF) and femoral mean thickness. Boxplots are case-wise distributions and brackets indicate paired Wilcoxon p -values; the dashed horizontal line marks a ratio of 1 (no L/M asymmetry).

femoral cartilage. Overall, the cross-dataset agreement of these simple anatomical signatures supports the validity of the automated segmentations and L/M partitions used for downstream radiomics.

6. Radiomics Results

6.1. Radiomic similarity between compartments

Spearman correlations between all features for every pair of ROIs and, for each pair, counted the number of features with $|\rho| \geq 0.7$. These counts are visualised as chord diagrams in Figure 7, where thicker chords indicate more strongly correlated features.

Across all three datasets we observed highly consistent patterns. Subchondral bone bands showed the strongest radiomic coupling: medial–lateral pairs within the same bone and tibial–femoral subchondral pairs shared the largest numbers of strongly correlated features.

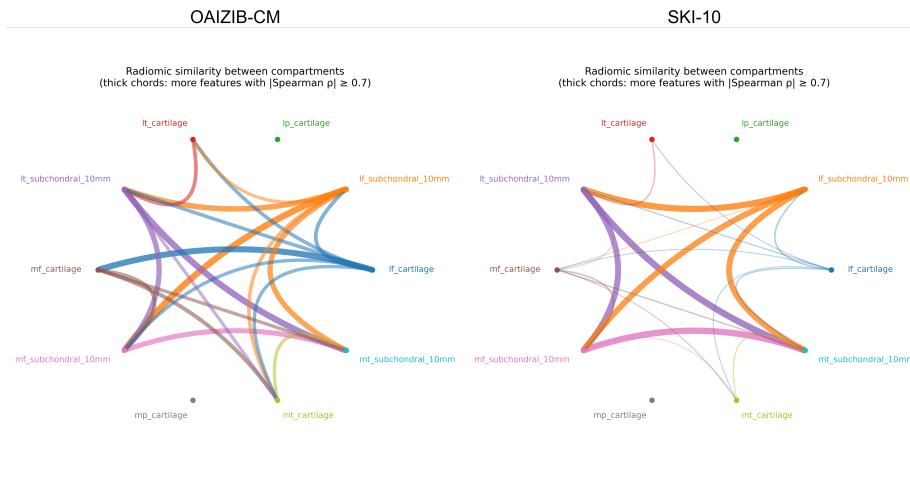


Figure 7: Radiomic similarity between knee compartments across datasets. Chord diagrams show pairwise Spearman correlations [46] between radiomic (right). Nodes correspond to cartilage and 10 mm subchondral bone bands; thicker chords indicate more features with $|\rho| \geq 0.7$ between a given pair of compartments.

similarity (LF–MF, LT–MT), and each cartilage was radiomically similar to its underlying subchondral band. In contrast, patellar cartilage (LP/MP) shared almost no strongly correlated features with tibiofemoral cartilage or subchondral bone, appearing nearly isolated in all three chord diagrams. These patterns suggest that tibial and femoral cartilage–bone units form tightly coupled radiomic compartments, whereas the patellofemoral compartment is radiomically distinct.

6.2. Relationship between ROI size and radiomic features

To assess how many radiomic features are essentially proxies for ROI size, we computed Spearman correlations between each feature and the corresponding ROI’s mean thickness and volume, separately for each dataset. For every ROI (465 features) we counted the number of features with strong correlation $|\rho| \geq 0.7$ with thickness or volume in Figure 8).

Across cohorts, only a minority of features showed such strong size-dependence. On average, 6–12% of features per ROI were strongly correlated with either

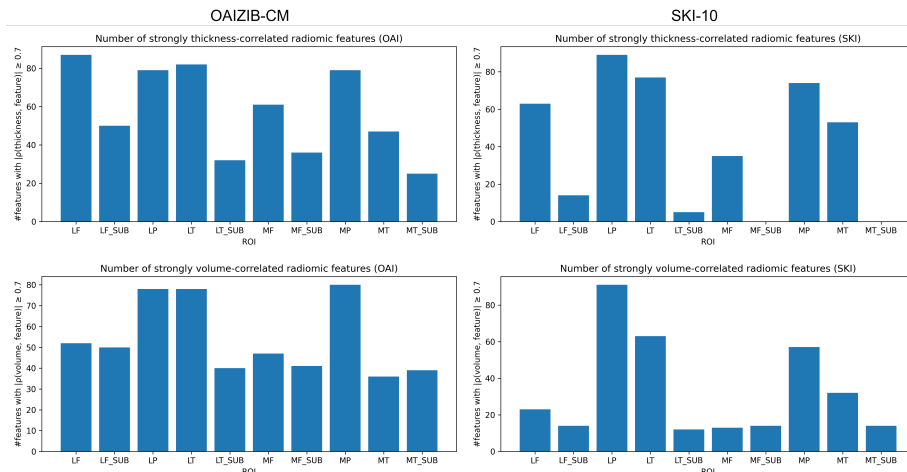


Figure 8: Number of radiomic features strongly correlated with ROI size. many of the 465 radiomic features have Spearman correlation $|\rho| \geq 0.7$ with mean thickness (top row) or volume (bottom row). Cartilage ROIs, especially patellar and tibial cartilage, exhibit more size-correlated features than subchondral bone bands, and thickness correlations generally exceed volume correlations.

thickness or volume, with slightly more features linked to thickness than to volume (mean proportion of thickness-correlated features 0.12 vs. 0.08 for volume across all ROIs and datasets). Cartilage ROIs were noticeably more size-dependent than subchondral bands: in OAI-ZIB-CM, cartilage had ~ 13 – 16% of features strongly correlated with thickness or volume, whereas the subchondral bands had only 7–9%; in SKI-10 and

The patellar cartilage (LP/MP) and tibial cartilage (LT/MT) consistently exhibited the largest numbers of size-correlated features (up to $\sim 90/465$ features in some datasets), indicating that a substantial subset of their texture descriptors reflects simple geometric differences. In contrast, femoral and tibial subchondral bands showed few strongly size-correlated features, suggesting that their radiomic profiles capture information that is less dominated by global thickness or volume. Overall, these analyses confirm that most radiomic features are not trivially explained by ROI size, while also identifying compartments and feature subsets in which size effects are more pronounced.

Table 5: OA vs non-OA classification performance (5-fold CV) on (volume/thickness-correlated) features. N_{feat} is the number of features used after LASSO.

Dataset / set	Model	N_{feat}	AUC	F1	Acc.	Rec.	Prec.
OAIZIB-CM	lasso	14	0.906	0.832	0.792	0.812	0.852
OAIZIB-CM	knn	14	0.868	0.827	0.772	0.859	0.797
OAIZIB-CM	svm_rbf	14	0.891	0.882	0.842	0.938	0.833
OAIZIB-CM	xgboost	14	0.849	0.833	0.782	0.859	0.809
OAIZIB-CM (volume/thickness)	lasso	4	0.777	0.752	0.673	0.781	0.725
OAIZIB-CM (volume/thickness)	knn	4	0.740	0.748	0.693	0.719	0.780
OAIZIB-CM (volume/thickness)	svm_rbf	4	0.768	0.760	0.693	0.766	0.754
OAIZIB-CM (volume/thickness)	xgboost	4	0.730	0.733	0.653	0.750	0.716

6.3. OA classification from radiomics versus size-linked features

We evaluated whether OA classification is mainly driven by simple size differences (volume/thickness) or by subtler radiomic patterns. For each

(i) a radiomics set obtained from our pipeline after univariate filtering and LASSO feature selection (*radiomics*); and

(ii) a size-linked set restricted to radiomic features that showed strong correlation with ROI volume or thickness ($|\text{Spearman } \rho| \geq 0.7$; *size-linked*). For both sets we trained four classifiers : LASSO logistic regression [45], k NN [47], RBF-SVM [48], XGBoost [49], in 5-fold stratified cross-validation and reported AUC, F1, accuracy, precision and recall in Table 5.

On OAIZIB-CM, the radiomics features achieved AUCs between 0.849 and 0.906 across models, with the best result for LASSO (AUC=0.906, Accuracy=0.79). Restricting the input to size-linked features reduced AUC to 0.730–0.777, i.e. a mean drop of 0.12–0.13 across models. AUCs of 0.732–0.827 (best: RBF-SVM, AUC=0.827, Accuracy=0.75), whereas size-linked features only reached 0.613–0.729 (mean AUC drop 0.07–0.15). ROC curves in Figure 9 illustrate this consistent performance gap.

To further probe size dependence, we examined the Spearman correlations between the LASSO-selected radiomic features and ROI volume/thickness in Figure 10. For the radiomics feature sets, most selected features showed only

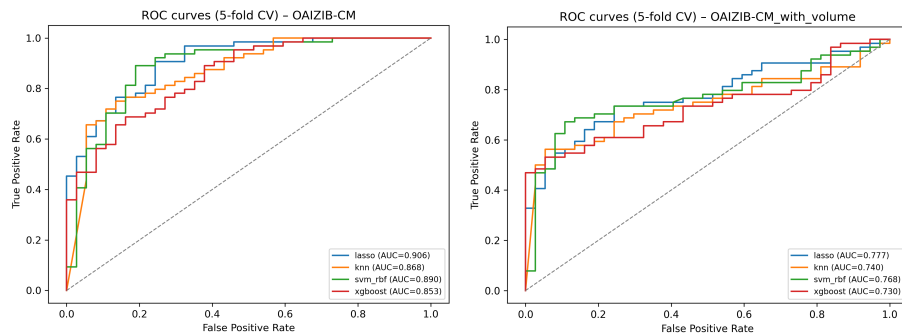


Figure 9: OA vs non-OA classification ROC curves (5-fold CV) on RBF-SVM, XGBoost). Left: models trained on LASSO-selected radiomic features; right: models trained on size-linked (volume/thickness- correlated) features only. Legends report the corresponding AUCs. In both cohorts, radiomic features consistently outperform size-linked features across all classifiers.

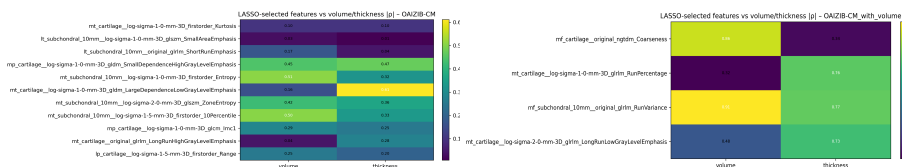


Figure 10: Correlation of LASSO-selected radiomic features with ROI size. Heatmaps show absolute Spearman correlations $|\rho|$ between each selected feature and its ROI volume/thickness for OAI ZIB-CM (top) and (*radiomics*); right: features selected when restricting the input to volume/thickness-correlated candidates (*with_volume*). Radiomics-selected features are only weakly size-dependent, whereas *with_volume* features are, by design, strongly correlated with ROI size.

modest correlation with size ($|\rho| \lesssim 0.3-0.4$), confirming that LASSO preferentially picks texture descriptors that are not simple surrogates of volume or thickness. In contrast, the features selected from the size-linked pools were, by construction, strongly correlated with size (many $|\rho| \geq 0.7$), yet they produced clearly inferior OA discrimination. Overall, these results indicate that our pipeline captures radiomic information beyond gross morphometric changes, and that this additional texture signal substantially improves OA vs non-OA classification over volume/thickness-driven features alone.

7. Discussion

In this work we introduced LM-CartSeg, an end-to-end framework that links state-of-the-art 3D nnU-Net segmentation with rule-based geometric post-processing, automated L/M partitioning and radiomics analysis of knee MRI. Across multiple public and clinical cohorts, the pipeline produced accurate, anatomically plausible ROIs for femoral, tibial and patellar cartilage and their 10 mm subchondral bone bands, and enabled systematic investigation of radiomic similarity, size dependence and OA classification. Compared with prior KOA radiomics studies that typically target either cartilage or subchondral bone in isolation and rely on manual delineation of a few compartments [9, 10, 11, 12, 13, 15, 16, 17], our approach offers fully automatic, multi-compartment ROIs that jointly represent cartilage–bone units and explicitly encode L/M anatomy.

The segmentation experiments highlight the value of combining nnU-Net with simple geometric rules. On both the in-domain OAIZIB-CM test set and the out-of-distribution SKI-10 dataset, post-processing substantially reduced ASSD and HD95 while preserving or slightly improving DSC. These gains reflect removal of small spurious components and smoothing of jagged surfaces, which are known to degrade surface-based metrics despite high voxelwise overlap. Importantly, we evaluated not only overlap but also the stability of the learned L/M partition. A direct L/M nnU-Net could recover the geometric split almost occasionally swapped sides or produced highly asymmetric boundary confusion. In contrast, our geometric L/M rule is deterministic, annotation-free and depends only on tibial shape and scanner left–right orientation, making it intrinsically robust to changes in intensity, sequence and OA severity. This suggests that for tasks where anatomical semantics are largely geometric—such as L/M partitioning—simple rules can outperform purely data-driven labels in terms of generalisability.

The anatomical QC analyses further support the validity of the generated ROIs. Across three datasets, medial tibial cartilage was consistently smaller and thinner than lateral cartilage, with medial–lateral thickness ratios around 0.86–

0.88 and differences of -0.25 to -0.30 mm, in line with known loading patterns and OA predilection of the medial compartment [50, 51]. Femoral cartilage exhibited near-symmetric volumes and thicknesses, with femoral thickness ratios close to 1 and mostly non-significant L/M differences [52]. These consistent patterns across heterogeneous cohorts argue against systematic L/M swapping or gross geometric artefacts, and illustrate how simple morphometric signatures can serve as practical QC indicators in large-scale automated pipelines.

Our radiomics analyses provide several insights into how cartilage and subchondral bone contribute to OA-related image phenotypes. First, chord diagrams showed that radiomic profiles of subchondral bands are strongly coupled within each bone and between tibial and femoral bands, whereas patellar cartilage appears radiomically isolated from tibiofemoral compartments. This supports the notion of bone–cartilage units as functional entities in OA and is consistent with subchondral bone radiomics studies that achieved strong discrimination between OA and non-OA knees [9, 10, 12]. Second, only a minority of features—typically 6–12% per ROI—were strongly correlated with volume or thickness, and correlations were weaker in subchondral bands than in cartilage. Thus, most radiomic descriptors capture texture patterns not trivially explained by global ROI size, particularly in bone.

The OA classification results reinforce this interpretation. Across both models restricted to volume/thickness-linked features, with AUC gains of roughly 0.1 or more across classifiers. Moreover, LASSO-selected features from the full radiomics sets were only weakly correlated with ROI size, whereas features selected from the size-linked pools remained strongly size-dependent and yielded inferior discrimination. Together, these findings indicate that our automated pipeline exposes meaningful texture information beyond simple morphometric changes, even when using routine clinical sequences rather than quantitative T_2 or $T_{1\rho}$ maps. In contrast to studies that integrate only a few radiomic features with clinical variables or deep features [11, 12, 13, 15], our work emphasises the interplay between segmentation robustness, anatomical QC and feature selection in determining the reliability and interpretability of OA radiomics.

Several limitations should be acknowledged. First, although we evaluated DESS-like OAIZIB-CM and SKM-TEA images; performance on other field strengths, vendors or sequences remains to be established. Second, the labels, which are noisy proxies rather than radiographic or arthroscopic standards. Third, our radiomics analysis is cross-sectional and focuses on binary OA classification; we did not investigate progression, pain trajectories or response to interventions. Fourth, we used hand-crafted radiomic features and classical machine-learning classifiers; more advanced approaches such as graph neural networks or end-to-end multi-task models might further improve performance but would also require larger, harmonised datasets. Finally, although we excluded shape features due to robustness concerns, we did not systematically assess test-retest repeatability or the impact of different discretisation schemes.

Moreover, our radiomics classification experiments were deliberately restricted to within-cohort training and validation, and we did not attempt to construct a cross-centre deployable OA classifier. Given the known sensitivity of hand-crafted radiomic features to acquisition protocols and scanners, robust multi-centre generalisation will likely require dedicated harmonisation or end-to-end deep learning approaches.

Future work will address these limitations by integrating longitudinal data, harmonising multi-centre acquisitions, and exploring hybrid models that combine LM-CartSeg ROIs with deep radiomic representations. The proposed geometric L/M rule and QC framework are generic and could be extended to other joints or imaging modalities, providing a reusable backbone for anatomically grounded radiomics in musculoskeletal imaging.

8. Conclusion

We developed LM-CartSeg, a fully automated pipeline that couples robust multi-structure segmentation with geometric L/M partitioning, anatomical QC and radiomics analysis of knee MRI. Across public and clinical cohorts, the method produced accurate cartilage and subchondral bone masks, improved

surface-based metrics via simple post-processing rules, and delivered deterministic L/M compartments that remained stable under domain shift.

Radiomics experiments showed that tibiofemoral cartilage–bone units share strong texture signatures, that most radiomic features are not simple surrogates of ROI size, and that OA vs. non-OA classification benefits substantially from texture-based features beyond volume and thickness. These results suggest that LM-CartSeg can serve as a practical foundation for large-scale, reproducible radiomics studies in knee osteoarthritis and may facilitate future work on early disease detection and progression prediction in routine clinical MRI.

Data and Code Availability

Declaration of competing interest

Acknowledgements

References

- [1] E. R. Vina, C. K. Kwok, Epidemiology of osteoarthritis: literature update, *Current opinion in rheumatology* 30 (2018) 160–167.
- [2] J. D. Steinmetz, G. T. Culbreth, L. M. Haile, Q. Rafferty, J. Lo, K. G. Fukutaki, J. A. Cruz, A. E. Smith, S. E. Vollset, P. M. Brooks, et al., Global, regional, and national burden of osteoarthritis, 1990–2020 and projections to 2050: a systematic analysis for the global burden of disease study 2021, *The Lancet Rheumatology* 5 (2023) e508–e522.
- [3] B. A. de Vries, S. J. Breda, B. Sveinsson, E. J. McWalter, D. E. Meuffels, G. P. Krestin, B. A. Hargreaves, G. E. Gold, E. H. Oei, Detection of knee synovitis using non-contrast-enhanced qdss compared with contrast-enhanced mri, *Arthritis Research & Therapy* 23 (2021) 55.
- [4] Y. Wang, A. E. Wluka, G. Jones, C. Ding, F. M. Cicuttini, Use magnetic resonance imaging to assess articular cartilage, *Therapeutic advances in musculoskeletal disease* 4 (2012) 77–97.

- [5] A. H. Gomoll, H. Yoshioka, A. Watanabe, J. C. Dunn, T. Minas, Preoperative measurement of cartilage defects by mri underestimates lesion size, *Cartilage* 2 (2011) 389–393.
- [6] G. Cao, S. Gao, B. Xiong, Application of quantitative t1, t2 and t2* mapping magnetic resonance imaging in cartilage degeneration of the shoulder joint, *Scientific Reports* 13 (2023) 4558.
- [7] P. Lambin, R. T. Leijenaar, T. M. Deist, J. Peerlings, E. E. De Jong, J. Van Timmeren, S. Sanduleanu, R. T. Larue, A. J. Even, A. Jochems, et al., Radiomics: the bridge between medical imaging and personalized medicine, *Nature reviews Clinical oncology* 14 (2017) 749–762.
- [8] J. E. Van Timmeren, D. Cester, S. Tanadini-Lang, H. Alkadhi, B. Baessler, Radiomics in medical imaging—“how-to” guide and critical reflection, *Insights into imaging* 11 (2020) 91.
- [9] J. Hirvasniemi, S. Klein, S. Bierma-Zeinstra, M. W. Vernooij, D. Schiphof, E. H. Oei, A machine learning approach to distinguish between knees without and with osteoarthritis using mri-based radiomic features from tibial bone, *European radiology* 31 (2021) 8513–8521.
- [10] Z. Xue, L. Wang, Q. Sun, J. Xu, Y. Liu, S. Ai, L. Zhang, C. Liu, Radiomics analysis using mr imaging of subchondral bone for identification of knee osteoarthritis, *Journal of Orthopaedic Surgery and Research* 17 (2022) 414.
- [11] T. Cui, R. Liu, Y. Jing, J. Fu, J. Chen, Development of machine learning models aiming at knee osteoarthritis diagnosing: an mri radiomics analysis, *Journal of Orthopaedic Surgery and Research* 18 (2023) 375.
- [12] J. Fu, L. Mu, D. Dong, M. Li, Z. Miao, X. Huai, Y. Zheng, H. Zhang, An mri-based radiomics framework for early identification and progression stratification in knee osteoarthritis: data from the osteoarthritis initiative, *BMC Musculoskeletal Disorders* 26 (2025) 1–10.

- [13] T. Chen, J. Chen, H. Liu, Z. Liu, B. Yu, Y. Wang, W. Zhao, Y. Peng, J. Li, Y. Yang, et al., Integration of longitudinal load-bearing tissue mri radiomics and neural network to predict knee osteoarthritis incidence, *Journal of Orthopaedic Translation* 51 (2025) 187–197.
- [14] F. Angelone, F. K. Ciliberti, H. Jónsson, M. K. Gíslason, M. Romano, A. Franco, F. Amato, P. Gargiulo, Knee cartilage degradation in the medial and lateral anatomical compartments: a radiomics study, in: *2024 IEEE international conference on metrology for eXtended reality, artificial intelligence and neural engineering (MetroXRaine)*, IEEE, 2024, pp. 183–188.
- [15] F. Angelone, F. K. Ciliberti, G. P. Tobia, H. Jónsson Jr, A. M. Ponsiglione, M. K. Gislason, F. Tortorella, F. Amato, P. Gargiulo, Innovative diagnostic approaches for predicting knee cartilage degeneration in osteoarthritis patients: a radiomics-based study, *Information Systems Frontiers* 27 (2025) 51–73.
- [16] T. Lin, S. Peng, S. Lu, S. Fu, D. Zeng, J. Li, T. Chen, T. Fan, C. Lang, S. Feng, et al., Prediction of knee pain improvement over two years for knee osteoarthritis using a dynamic nomogram based on mri-derived radiomics: a proof-of-concept study, *Osteoarthritis and cartilage* 31 (2023) 267–278.
- [17] Y. Xie, Y. Dan, H. Tao, C. Wang, C. Zhang, Y. Wang, J. Yang, G. Yang, S. Chen, Radiomics feature analysis of cartilage and subchondral bone in differentiating knees predisposed to posttraumatic osteoarthritis after anterior cruciate ligament reconstruction from healthy knees, *BioMed Research International* 2021 (2021) 4351499.
- [18] F. Isensee, P. F. Jaeger, S. A. Kohl, J. Petersen, K. H. Maier-Hein, nnu-net: a self-configuring method for deep learning-based biomedical image segmentation, *Nature methods* 18 (2021) 203–211.
- [19] C. G. Chadoulos, D. E. Tsaopoulos, S. Moustakidis, N. L. Tsakiridis, J. B.

- Theocharis, A novel multi-atlas segmentation approach under the semi-supervised learning framework: Application to knee cartilage segmentation, *Computer Methods and Programs in Biomedicine* 227 (2022) 107208.
- [20] S. Khan, B. Azam, Y. Yao, W. Chen, Deep collaborative network with alpha matte for precise knee tissue segmentation from mri, *Computer Methods and Programs in Biomedicine* 222 (2022) 106963.
- [21] F. Isensee, T. Wald, C. Ulrich, M. Baumgartner, S. Roy, K. Maier-Hein, P. F. Jaeger, nnu-net revisited: A call for rigorous validation in 3d medical image segmentation, in: *International Conference on Medical Image Computing and Computer-Assisted Intervention*, Springer, 2024, pp. 488–498.
- [22] W. Lv, J. Peng, J. Hu, Y. Lu, Z. Zhou, H. Xu, K. Xing, X. Zhang, L. Lu, Lmsst-gen: Longitudinal mri sub-structural texture guided graph convolution network for improved progression prediction of knee osteoarthritis, *Computer Methods and Programs in Biomedicine* 261 (2025) 108600.
- [23] F. Ambellan, A. Tack, M. Ehlke, S. Zachow, Automated segmentation of knee bone and cartilage combining statistical shape knowledge and convolutional neural networks: Data from the osteoarthritis initiative, *Medical image analysis* 52 (2019) 109–118.
- [24] Y. Yao, J. Zhong, L. Zhang, S. Khan, W. Chen, Cartimorph: A framework for automated knee articular cartilage morphometrics, *Medical Image Analysis* 91 (2024) 103035.
- [25] W. Wirth, O. Benichou, C. K. Kwok, A. Guermazi, D. Hunter, R. Putz, F. Eckstein, O. Investigators, Spatial patterns of cartilage loss in the medial femoral condyle in osteoarthritic knees: data from the osteoarthritis initiative, *Magnetic resonance in medicine* 63 (2010) 574–581.
- [26] R. K. Surowiec, E. P. Lucas, E. K. Fitzcharles, B. M. Petre, G. J. Dornan, J. E. Giphart, R. F. LaPrade, C. P. Ho, T2 values of articular cartilage

- in clinically relevant subregions of the asymptomatic knee, *Knee Surgery, Sports Traumatology, Arthroscopy* 22 (2014) 1404–1414.
- [27] E. Panfilov, A. Tiulpin, M. T. Nieminen, S. Saarakkala, V. Casula, Deep learning-based segmentation of knee mri for fully automatic subregional morphological assessment of cartilage tissues: data from the osteoarthritis initiative, *Journal of Orthopaedic Research* 40 (2022) 1113–1124.
- [28] A. D. Desai, A. M. Schmidt, E. B. Rubin, C. M. Sandino, M. S. Black, V. Mazzoli, K. J. Stevens, R. Boutin, C. Ré, G. E. Gold, et al., Skm-tea: A dataset for accelerated mri reconstruction with dense image labels for quantitative clinical evaluation, *arXiv preprint arXiv:2203.06823* (2022).
- [29] A. Carré, G. Klausner, M. Edjlali, M. Lerousseau, J. Briend-Diop, R. Sun, S. Ammari, S. Reuzé, E. Alvarez Andres, T. Estienne, et al., Standardization of brain mr images across machines and protocols: bridging the gap for mri-based radiomics, *Scientific reports* 10 (2020) 12340.
- [30] A. Zwanenburg, M. Vallières, M. A. Abdalah, H. J. Aerts, V. Andrearczyk, A. Apte, S. Ashrafinia, S. Bakas, R. J. Beukinga, R. Boellaard, et al., The image biomarker standardization initiative: standardized quantitative radiomics for high-throughput image-based phenotyping, *Radiology* 295 (2020) 328–338.
- [31] A. Dovrou, K. Nikiforaki, D. Zaridis, G. C. Manikis, E. Mylona, N. Tachos, M. Tsiknakis, D. I. Fotiadis, K. Marias, A segmentation-based method improving the performance of n4 bias field correction on t2weighted mr imaging data of the prostate, *Magnetic Resonance Imaging* 101 (2023) 1–12.
- [32] H. Hotelling, Analysis of a complex of statistical variables into principal components., *Journal of educational psychology* 24 (1933) 417.
- [33] J. MacQueen, Multivariate observations, in: *Proceedings of the 5th Berkeley*

- ley Symposium on Mathematical Statistics and Probability, volume 1, 1967, pp. 281–297.
- [34] N. Hafezi-Nejad, A. Guermazi, F. W. Roemer, D. J. Hunter, E. B. Dam, B. Zikria, C. K. Kwok, S. Demehri, Prediction of medial tibiofemoral compartment joint space loss progression using volumetric cartilage measurements: data from the fnih oa biomarkers consortium, *European radiology* 27 (2017) 464–473.
- [35] T. Heimann, B. J. Morrison, M. A. Styner, M. Niethammer, S. Warfield, Segmentation of knee images: a grand challenge, in: *Proc. MICCAI Workshop on Medical Image Analysis for the Clinic*, volume 1, Beijing, China, 2010.
- [36] L. R. Dice, Measures of the amount of ecologic association between species, *Ecology* 26 (1945) 297–302.
- [37] T. Heimann, B. Van Ginneken, M. A. Styner, Y. Arzhaeva, V. Aurich, C. Bauer, A. Beck, C. Becker, R. Beichel, G. Bekes, et al., Comparison and evaluation of methods for liver segmentation from ct datasets, *IEEE transactions on medical imaging* 28 (2009) 1251–1265.
- [38] J. Fournel, A. Bartoli, D. Bendahan, M. Guye, M. Bernard, E. Rauseo, M. Y. Khanji, S. E. Petersen, A. Jacquier, B. Ghattas, Medical image segmentation automatic quality control: A multi-dimensional approach, *Medical Image Analysis* 74 (2021) 102213.
- [39] J. Guo, P. Yan, Y. Qin, M. Liu, Y. Ma, J. Li, R. Wang, H. Luo, S. Lv, Automated measurement and grading of knee cartilage thickness: a deep learning-based approach, *Frontiers in Medicine* 11 (2024) 1337993.
- [40] B. Spektor-Fadida, L. Ben-Sira, D. Ben-Bashat, L. Joskowicz, Segqc: a segmentation network-based framework for multi-metric segmentation quality control and segmentation error detection in volumetric medical images, *Medical Image Analysis* (2025) 103638.

- [41] A. Peuna, J. Hekkala, M. Haapea, J. Podlipská, A. Guermazi, S. Saarakkala, M. T. Nieminen, E. Lammentausta, Variable angle gray level co-occurrence matrix analysis of t2 relaxation time maps reveals degenerative changes of cartilage in knee osteoarthritis: Oulu knee osteoarthritis study, *Journal of Magnetic Resonance Imaging* 47 (2018) 1316–1327.
- [42] B. R. Kim, H. J. Yoo, H.-D. Chae, S. H. Hong, J.-Y. Choi, Fat-suppressed t2 mapping of human knee femoral articular cartilage: comparison with conventional t2 mapping, *BMC musculoskeletal disorders* 22 (2021) 662.
- [43] J. J. Van Griethuysen, A. Fedorov, C. Parmar, A. Hosny, N. Aucoin, V. Narayan, R. G. Beets-Tan, J.-C. Fillion-Robin, S. Pieper, H. J. Aerts, Computational radiomics system to decode the radiographic phenotype, *Cancer research* 77 (2017) e104–e107.
- [44] L. Duron, D. Balvay, S. Vande Perre, A. Bouchouicha, J. Savatovsky, J.-C. Sadik, I. Thomassin-Naggara, L. Fournier, A. Lecler, Gray-level discretization impacts reproducible mri radiomics texture features, *PLoS One* 14 (2019) e0213459.
- [45] R. Tibshirani, Regression shrinkage and selection via the lasso, *Journal of the Royal Statistical Society Series B: Statistical Methodology* 58 (1996) 267–288.
- [46] A. Rovetta, Raiders of the lost correlation: a guide on using pearson and spearman coefficients to detect hidden correlations in medical sciences, *Cureus* 12 (2020).
- [47] T. Cover, P. Hart, Nearest neighbor pattern classification, *IEEE transactions on information theory* 13 (1967) 21–27.
- [48] B. Schölkopf, A. J. Smola, *Learning with kernels: support vector machines, regularization, optimization, and beyond*, MIT press, 2002.

- [49] T. Chen, C. Guestrin, Xgboost: A scalable tree boosting system, in: Proceedings of the 22nd acm sigkdd international conference on knowledge discovery and data mining, 2016, pp. 785–794.
- [50] R. F. Shah, A. M. Martinez, V. Pedoia, S. Majumdar, T. P. Vail, S. A. Bini, Variation in the thickness of knee cartilage. the use of a novel machine learning algorithm for cartilage segmentation of magnetic resonance images, *The Journal of arthroplasty* 34 (2019) 2210–2215.
- [51] M. P. Jansen, S. C. Mastbergen, J. W. MacKay, T. D. Turmezei, F. Lafeber, Knee joint distraction results in mri cartilage thickness increase up to 10 years after treatment, *Rheumatology* 61 (2022) 974–982.
- [52] G. Giurazza, C. Caria, S. Campi, E. Franceschetti, G. F. Papalia, S. Bas-ciani, A. Zampoli, P. Gregori, R. Papalia, A. Marinozzi, Femoral cartilage thickness measured on mri varies among individuals: Time to deepen one of the principles of kinematic alignment in total knee arthroplasty. a systematic review, *Knee Surgery, Sports Traumatology, Arthroscopy* 33 (2025) 634–645.